Proceedings World Geothermal Congress 2015
Melbourne, Australia, 19-25 April 2015

Modelling Viscous Fingering during Reinjection in Geothermal Reservoirs

Alastair MCDOWELL, Sadiq J. ZARROUK* and Richard CLARKE

Department of Engineering Science, the University of Auckland, New Zealand

*s.zarrouk@auckland.ac.nz

Keywords: Viscous Fingering, Hydrodynamic Instability, Reinjection, Geothermal Reservoirs, TOUGH2.2 Simulator

ABSTRACT

Viscous fingering is a hydrodynamic instability that can be caused by a viscosity difference across a travelling thermal front. The equations governing the instability of radial flow through porous media are cast, and a linear perturbation analysis was performed numerically. Transient growth of temperature perturbations show which wave number, and hence fingering displacement shape, will be most unstable. Results illustrate that there are two parameters that define the stability: the Péclet number and the log-mobility ratio (for homogeneous media). These critical parameters provide limits on reinjection temperature and flow rate for a given reservoir temperature that will cause thermal stability. In addition, the TOUGH2.2 numerical simulator was used to model fluid flow displacement patterns that occur during reinjection in geothermal reservoirs. Results show that a critical Péclet number and log-mobility ratio exist for the onset of viscous fingering. Moreover, in cases where the porous medium is heterogeneous, fingering displacements are dominated by the permeability structure for heterogeneity indices beyond some critical value (the precise value of which should factor in inherent numerical dispersion present in the TOUGH2.2 simulator.

1. INTRODUCTION

Reinjection is a vital process in geothermal field management as it provides pressure support, reduces/mitigates subsidence, and at the same time it is an environmentally friendly way for disposal of waste fluid (Kaya et al. 2011).

Viscous fingering is a hydrodynamic instability phenomenon that occurs in porous media during the displacement of fluids having different viscosities. The occurrence of viscous fingering is of particular interest to geothermal reservoir engineers during the re-injection of hot brine or cold condensates. Fingering can cause negative effects if it results in thermal breakthrough, which can affect production and field operation (Kaya et al. 2011).

Viscous fingering phenomena have been studied with much interest by many authors dating back to its earliest discovery in 1958. Saffman and Taylor (1958) found that when a less viscous fluid is driven into a porous medium with pores saturated by a more viscous fluid, the planar interface between the liquids was shown to be liable to instability. Saffman and Taylor (1958) found through experiments that a similar result is observed when less viscous fluid is injected between two closely spaced glass sheets of a Hele-Shaw cell filled with a more viscous fluid.

Reinjection in geothermal reservoirs typically involves a point injection source. Hence we are more interested in a polar coordinate formulation to model a radial source flow. Tan and Homsy (1987) made the distinction between rectilinear and radial flow that the base state for radial flow change spatially as the interface moves outwards, whereas for a rectilinear analysis, base state velocity is constant (does not change spatially). This has important implications on the growth rate of perturbation to the base states.

Linear stability analysis is a common methodology used by many authors to determine whether small perturbations on state variables grow or decay over time (Kim 2012; Islam and Azaiez 2010a; Pritchard 2004; Tan and Homsy 1987). Linear stability analysis results are only valid for the initial onset of instability, after which non-linear effects dominate.

Tan and Homsy (1987) pointed out that there are two non-dimensional parameters that determine the stability of a radial source flow. Firstly the Péclet number which measures the ratio of the rate of thermal advection to diffusion, and is defined by reservoir material properties and the mass injection rate. Secondly, the log-mobility ratio, which is the difference between the viscosities of the injected fluid and that of the fluid within the reservoir, they also derived a linear stability formulation based on two different fluids with different viscosities. Governing equations are cast in terms of isothermal mass diffusion. In the geothermal reservoir context we are interested in thermal diffusion of two identical fluids with viscosities strongly dependent on temperature, rather than concentration of different fluid species, though the approach is very similar.

Viscous fingering is a well-known phenomenon in reservoir engineering, first discovered in the petroleum industry. In oil reservoirs, immiscible viscous fingering is observed during the process of enhanced oil recovery (Sajjadi and Azaiez, 2012). The sharp interface arises from difference in polarity between the injection fluid, water, and oil.

Few authors have addressed the subject of viscous fingering in relation to geothermal systems. Fitzgerald and Shook (1994) uses the geothermal simulator TETRAD to model reinjection of liquid into a porous layer containing superheated vapour. There is a dominant type of fingering formation that occurs in homogeneous reservoirs having uniform permeability and thermal properties. However, the displacement patterns show sensitivities to the finite difference scheme used. This is a demonstration of the grid-orientation effect (GOE), studied in further detail by Chen et al. (1993a). According to Fitzgerald and Shook (1994), rapid injection schemes are inefficient due to inertial effects. In slow regimes, conduction dominates other heat transfer processes. Their work finds that a lower flow rate is more likely to stimulate fingering than a higher flow rate, thus a lower bound to flow rate is identified. However, this result is only valid for vapour dominated geothermal systems.

Peaceman and Rachford (1962) use a reservoir simulator based on a finite difference formulation when modeling a petroleum reservoir. They found that grid-orientation error dampens fingering perturbations, due to the numerical dispersion introduced in approximating derivatives over the sharp fronts. However, small perturbations to permeability are sufficient to initiate fingering. This leads to the field of heterogeneous fingering; a topic studied by many later authors.

Tan and Homsy (1988) acknowledge the shortcomings of the finite difference method, and develop a numerical simulation tool using the Spectral Method. This approach allows for a high degree of accuracy in approximating spatial derivatives, and consequently reduced numerical dispersion. Sajjadi and Azaiez (2012) also developed a pseudo-spectral numerical model suitable for investigating a fingering stability in a simple model of heterogeneity.

Reservoir heterogeneity has a large influence on the unstable displacement patterns that occur during reinjection. Tan and Homsy (1992) modeled the heterogeneities as a stationary random distribution, and varied the correlation length scale and variance of the permeability perturbations. There is a close coupling between homogeneous fingering, but preferential flow paths dominate as the variance is increased. Araktingi and Orr Jr (1993) studied fingering in heterogeneous media by implementing a particle tracking algorithm to numerically model mass dispersion. A heterogeneity index clearly defines the conditions that give rise to each type of fingering, including a transition region. Riaz and Meiburg (2004) studied a periodic permeability field. A transition from flow dominated by viscous fingering to flow dominated by the spatial permeability distribution is identified.

This work investigates the onset criteria for this viscous instability. This is studied analytically with the theory of linear stability analysis. The resulting criteria were then applied to numerical models for verification using the TOUGH2.2 geothermal reservoir simulator.

2. ANALYTICAL SOLUTION

2.1 Problem Formulation

To understand the process of radial viscous fingering in porous media, a simple analytical model is developed, incorporating known factors that may influence the instability.

In this section we will derive analytical results describing the physical process of viscous fingering in a geothermal reservoir due to high enthalpy reinjection inducing a viscosity contrast. A single fluid, water, has varying temperature along the radial direction. Governing equations of the flow are presented. Non-dimensionalisation allows influential parameters to be collected to form several non-dimensional numbers. A linear stability analysis on the resulting set of equations is used to determine under which circumstances a perturbation to the system will continue to grow. Transient growth rates of the perturbations are found numerically, showing which reinjection conditions are likely to be unstable at short times.

2.2 Thermal Front Stability Problem

Many studies have been undertaken for isothermal displacements in porous media, focusing on the instability of position of the fluid front. However, when fluid is injected into a porous medium saturated with the same fluid, but with a large temperature difference, a single thermal front develops. By contrast, this subject has been little studied, with notable contributions by Pritchard (2004) and Islam and Azaiez (2010a). The problem formulation described is designed to imitate a geothermal reinjection problem.

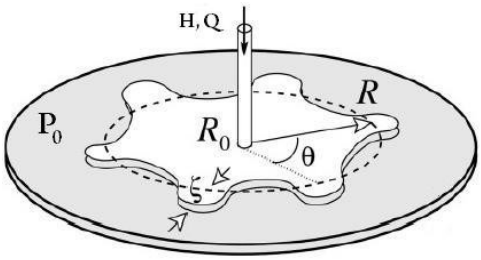

Figure 1: Schematic of analytical formulation. The thermal front displays a θ dependent instability of amplitude ζ (Dias and Miranda 2011).

Figure 1 depicts a fluid injected at volume flux rate Q with enthalpy H, which defines the total amount of energy in the fluid. At this enthalpy, fluid viscosity μ, density ρ_f and temperature T are found in steam tables. Reservoir pressure P_0, permeability k, rock density ρ_s, rock specific heat Cp_s, and porosity ϕ are known uniform parameters for a specific reservoir.

The equations governing the flow of the injectate through the reservoir are those of mass conservation, Darcy's Law for a porous media, and advection-diffusion of temperature. Here we use a Polar Coordinate system, (r, θ), centered at point of injection with radial and azimuthal components of velocity given by u_r and u_θ, respectively.

$$\nabla \cdot \mathrm{u} = 0$$

$$\frac{1}{r}\frac{\partial}{\partial r}(ru_r) + \frac{1}{r}\frac{\partial u_\theta}{\partial \theta} = 0 \tag{1}$$

The first expression is the usual statement of mass conservation, whilst the second is Darcy's Law, which gives the constitutive equation linking the velocity and pressure fields through reservoir permeability and fluid viscosity:

$$\frac{\partial p}{\partial r} = -\frac{\mu}{k}u_r \qquad \frac{1}{r}\frac{\partial p}{\partial \theta} = -\frac{\mu}{k}u_\theta \tag{2}$$

The advection-diffusion equations for temperature are:

$$\frac{\partial T}{\partial t} + \frac{\lambda}{\phi}\nabla\cdot(\mathrm{uT}) = \mathrm{D_T}\nabla^2 T \tag{3}$$

where ϕ is the porosity which is the ratio of pore to rock volume in the rock matrix. Porosity determines the thermal lag coefficient for given fluid and rock properties. Separate thermal and fluid fronts form as the rock matrix absorbs heat from the injected fluid, delaying the thermal boundary layer from the fluid front (Pritchard 2004). Thus, we hypothesise that by increasing reservoir porosity, the rock matrix has less of a stabilising influence on the instability.

Thermal diffusivity D_T pre-multiples the diffusion term in equation (3). Thermal diffusivity depends upon reservoir averaged rock and fluid properties of thermal conductivity K, density ρ, specific heat C_p (Çengel et al. 2012).

$$D_T = \frac{K}{\rho Cp} \tag{4}$$

The specific heat C_p is the specific heat of the rock matrix is a significant factor influencing the formation of viscous fingering. The volumetric heat capacity (thermal capacity) ρCp determines the ability of rock to store heat. A large volumetric heat capacity can retard the thermal front by reducing the thermal diffusivity, thus allowing advective processes to dominate.

The thermal lag coefficient λ (non-dimensional) introduced by Jupp and Woods (2003) quantifies the retardation of the thermal front due to the necessary heat transfer to the porous rock matrix in the reservoir:

$$\lambda = \frac{\phi\rho_f Cp_f}{\phi\rho_f Cp_f + (1-\phi)\rho_s Cp_s} \tag{5}$$

Equation 5 takes into account the volume fraction of rock (*s*) and fluid (*f*) defined by the porosity ϕ of the rock, with subscripts defined accordingly..

2.2.1 Assumptions

It is assumed that the Darcy's Law does apply to this problem. Rock and fluid are treated as being in local equilibrium (O'Sullivan and Pruess 1980). Capillary pressure is a negligible effect. A constant permeability and porosity field is assumed for the linear stability portion of the study. Various heterogeneous permeability fields will be introduced later in section 3. Thermal diffusion is taken to be isotropic. All reservoir fluids remain in the liquid state, thus density can be taken as constant, yielding the simplified version of the continuity equation. Reservoir fluids are assumed incompressible. A constant injection rate and injection enthalpy is assumed. We will be using a 2D reservoir model with perturbations only considered in the azimuthal direction (using a polar coordinate system centered on the injection well).

2.2.2 Non Dimensionalisation

We first transform the governing dimensional equations into non-dimensional form. The choice of parameters by which to scale the equations must be made carefully. The geothermal reservoir is effectively infinite in planar extent and thus has no obvious length scale. Among the parameters: Q ($m^2\ s^{-1}$), $D_T D$ ($m^2\ s^{-1}$), k (m^2), $\mu 1$ ($kg\ m^{-1}\ s^{-1}$), T (ºC), H ($kJ\ kg^{-1}$), the only parameter exhibiting a length scale is the permeability. (Subscript 1 refers to the injection state.) Thus the root of permeability is the chosen length scale.

Non-dimensional variables are denoted with an asterisk.

$$r^* = r/k^{1/2}, \qquad t^* = tQ/k, \qquad u^* = uk^{1/2}/Q$$

$$T^* = (T-T_1)/(T_\infty - T_1), \qquad \mu^* = \mu/\mu_1, \qquad p^* = pk/\mu_1 Q \tag{6}$$

where T_∞ is the temperature of the native reservoir fluid and T_1 in the injected fluid temperature.

The governing equations of continuity 1, pressure 2, and advection-diffusion 3 can now be scaled by these non-dimensionalised variables. The new equations are therefore:

$$\frac{1}{r^*}\frac{\partial}{\partial r^*}(R^* u_r^*) + \frac{1}{r^*}\frac{\partial u^*_\theta}{\partial \theta} = 0 \tag{7}$$

$$\frac{\partial p^*}{\partial r^*} = -\mu u_r^* \qquad \frac{1}{r^*}\frac{\partial p^*}{\partial \theta} = -\mu u_\theta^* \tag{8}$$

$$\frac{\partial T*}{\partial t*}+\lambda\left[\frac{1}{r*}\frac{\partial(r*u*_r T*)}{\partial r*}+\frac{1}{r*}\frac{\partial(u_\theta T*)}{\partial\theta}\right]=\frac{1}{Pe_T}\left[\frac{1}{r*}\frac{\partial}{\partial r*}\left(r*\frac{\partial T*}{\partial r*}\right)+\frac{1}{(r*)^2}\frac{\partial^2 T*}{\partial\theta^2}\right] \tag{9}$$

The *Péclet Number* is the ratio of convective to diffusive terms governing the evolution of the thermal front. The thermal Péclet number is defined as

$$Pe_T=\frac{Q}{D_T} \tag{10}$$

From now on all variables are non-dimensionalised so asterisks are dropped for notational simplicity.

2.2.3 Basic State

To find the basic state of the stable, non-oscillating system, we must assume the basic state is independent of the azimuthal direction θ. Assuming a basic velocity state: $u_B=(1/r,0)$. Thus equation (9) reduces to:

$$\frac{\partial T}{\partial t}+\lambda\left[\frac{1}{r}\frac{\partial T}{\partial r}\right]=\frac{1}{Pe_T}\left[\frac{1}{r}\frac{\partial}{\partial r}\left(r\frac{\partial T}{\partial r}\right)\right] \tag{11}$$

Woods and Fitzgerald (1997) have found the basic state to be self-similar for the case of a constant injection rate. Riaz and Meiburg (2003) and Tan and Homsy (1987) both advocate the following similarity co-ordinate ξ to track the travelling thermal front.

$$\xi=r\sqrt{Pe_T/2t} \tag{12}$$

Transforming radial and temporal derivatives using chain rule gives

$$\frac{\partial}{\partial T}=-\frac{\xi}{2t}\frac{\partial}{\partial\xi},\qquad \frac{\partial}{\partial r}=\sqrt{\frac{Pe_T}{2t}}\frac{\partial}{\partial\xi} \tag{13}$$

Applying the similarity variable transformation, the partial differential equation is reduced in order to an ordinary differential equation in terms of only the similarity variable:

$$\frac{dT}{d\xi}\left(\frac{\lambda Pe_T-1}{\xi}-\xi\right)=\frac{d^2T}{d\xi^2} \tag{14}$$

Separating variables and integrating twice yields:

$$T_B(\xi(r,t))=A_1\int_0^\xi s^{\lambda Pe_T-1}e^{-\frac{s^2}{2}}ds \tag{15}$$

where A_1 is a constant.

Far field boundary conditions can be imposed to force temperature and pressure as r → ∞ to be the native reservoir conditions. Near the origin, r ≈ 0, the temperature is defined by the injection fluid. A singularity exists at r = 0, thus a small well-bore radius is assumed. In non-dimensional form, boundary conditions at the origin are T=0 and limr→0 $r.u_r$ = 1. Far field boundary conditions are T → 1 as r → ∞. Applying these boundary conditions gives the fully defined basic temperature state:

$$T_B(\xi(r,t))=\frac{\int_0^\xi s^{Pe_T\lambda-1}e^{-\frac{s^2}{2}}ds}{\int_0^\infty s^{Pe_T\lambda-1}e^{-\frac{s^2}{2}}ds} \tag{16}$$

The integral on the numerator is difficult to solve numerically for the large Péclet numbers which are prevalent in a typical geothermal scenario. Tan and Homsy (1987) introduces a new variable $w=\xi-(Pe_T\lambda)^{1/2}$, which rescales the position of the mean interface to w=0. This allows for an approximation to the basic temperature state at large Pe_T, permitting stable numerical simulations at these extremes. The approximation for $Pe_T\gg10$ is:

$$T_B(\xi(r,t))=\frac{1}{2}\left[1-erf\left\{\xi-(Pe_T\lambda)^{1/2}\right\}\right]+\vartheta(Pe_T^{-1/2}) \tag{17}$$

where *erf* is the error function, which is seen to have errors of order $Pe_T^{-1/2}$.

Viscosity is strong function of temperature for water. Tan and Homsy (1987) use an exponential relationship accounting for this temperature dependence.

$$\mu = e^{-RT} \tag{18}$$

where R is the log-mobility ratio defined as:

$$R = \ln \frac{\mu_\infty}{\mu_1} \tag{19}$$

where μ_1 is the dynamic viscosity of the injected fluid, μ_∞ is the dynamic viscosity of the native reservoir fluid. These viscosities are determined by the enthalpy of the injected fluid and temperature of native fluid.

2.3 Linear Stability Analysis

A linear stability analysis allows us to gauge the stability of the thermal front that forms during radial re-injection in a geothermal reservoir. Due to the base state varying in space and time, the classical quasi-steady state approximation (QSSA) cannot be taken. Thus, perturbations do not grow exponentially, but rather algebraically Tan and Homsy (1987). Thus the perturbations must be time stepped numerically, and here we choose to do that using the Method of Lines.

Small perturbations are taken about the basic states in the form: $\mathbf{u} = \mathbf{u_B} + \epsilon \mathbf{u}'$. The perturbed quantities are expanded in a series of normal modes in the azimuthal direction θ with wavenumber m. The small parameter is defined $\epsilon \ll 1$

$$(u_r, u_\theta, T', \mu, p')(r,\theta,t) = \left\{\hat{U}, \hat{V}, \hat{T}, \hat{M}, \hat{P}\right\} \exp(im\theta) \qquad m \mid \in Z \tag{20}$$

The subscript B refers to a basic state, and capitalised variables with superscript ∧ refer to the perturbed variable, which are functions of time and the radial direction.

Equation 7 and 8 are perturbed giving the following equation at order $\mathcal{O}(\in)$:

$$\frac{1}{r}\frac{\partial}{\partial r}(r\hat{U}) + \frac{im}{r}\hat{V} = 0 \tag{21}$$

$$\frac{\partial \hat{P}}{\partial r} = -\mu_B \hat{M} - \mu_B \hat{U} \tag{22}$$

$$\frac{im}{r}\hat{P} = -\mu_B \hat{M} - \mu_B \hat{V} \tag{23}$$

The constitutive equation 18 that links viscosity exponentially to temperature can also be perturbed and expanded in epsilon to give at $\mathrm{O}(\in)$:

$$\mu = \mu_B + \in e^{im\theta} \mu_B \left[-R\hat{T}\right] \tag{24}$$

Thus,

$$\mathcal{O}(\in): \hat{M} = \mu_B + \in e^{im\theta} \mu_B \left[-R\hat{T}\right] \tag{25}$$

When perturbing the temperature advection-diffusion equation 9, it is worth noting the basic velocity state is substituted $\mathbf{u} = (1/r, 0)$.

$$\mathcal{O}(\in): \frac{\partial \hat{T}}{\partial t} = \frac{1}{Pe_T}\left[\frac{1}{r}\frac{\partial}{\partial r}\left(r\frac{\partial \hat{T}}{\partial r}\right) - \frac{m^2}{r^2}\hat{T}\right] - \lambda\left[\frac{1}{r}\frac{\partial \hat{T}}{\partial r} + \hat{U}\frac{\partial T_B}{\partial r}\right] \tag{26}$$

Equations 21-26 can be combined by eliminating pressure $\hat{P}$ and tangential velocity $\hat{V}$ to yield an equation linking perturbations to the velocity field with perturbations to temperature:

$$\left(\frac{\partial}{\partial r}\left[r^2\mu_B\frac{\partial}{\partial r}+r\mu_B\right]-\mu_B m^2\right)\hat{U}=\left(-\frac{m^2}{r}\mu_B R\right)\hat{T} \tag{27}$$

2.3.1 Numerical Solution

The system has now been reduced to two coupled partial differential equations, equations 26 and 27 for $\hat{T}$ and $\hat{U}$ respectively. The Method of Lines is used to solve the system of equations. The radial direction is discretised and the vectors $\hat{\boldsymbol{U}}$ and $\hat{\boldsymbol{T}}$ contain the values of radial velocity and temperature at the computational nodes.The solution yields the time and radial varying coefficients to the perturbed states. For each wave number m, the growth rate of these solutions is measured (see Eqns 31-32 below), allowing the most unstable modes to be determined. Upon discretising the radial derivatives of $\hat{U}$ using central and upwind finite differencing, a matrix equation can be solved to yield $\hat{U}$ in terms of $\hat{T}$. Equation (26) yields the system of ODE's

$$\frac{\partial\hat{T}}{\partial t}+M_1\hat{U}=M_2\hat{T} \tag{28}$$

where matrices $\boldsymbol{M_1}$ and $\boldsymbol{M_2}$ contains the finite difference stencil for the differential operator on the left and right-hand side of Equation 26, respectively. Equation 27 gives a further relationship between $\hat{U}$ and $\hat{T}$

$$\hat{U}=M_U{}^{-1}\left[M_T\hat{T}\right] \tag{29}$$

where $\boldsymbol{M_U}$, $\boldsymbol{M_T}$ are matrices containing finite difference coefficients for the differential operators on the left- and right-hand side of Equation (27), respectively. This allows us to write down a single system of ODE's for $\hat{T}$ alone, which can be solved numerically in MATLAB using the built in ODE45 routine. Boundary conditions for the perturbations are $\hat{T}, r\hat{U}\rightarrow 0$ as $r\rightarrow 0,\infty$. The initial condition for the temperature and solute perturbations is an arbitrary Gaussian pulse that satisfies the boundary conditions:

$$\hat{T}(r,0)=\exp\left\{-\frac{(r-(Pe_T\lambda)^{1/2})^2}{c^2}\right\} \tag{30}$$

where c is the standard deviation

The thermal growth rate is an integrated quantity over the temperature perturbation field. We are undertaking a transient growth simulation, thus an integrated growth rate must be calculated at all points in time. The form of the energy norm used here is:

$$K(t)=\int_0^\infty \hat{T}(r,T)^2\,dr \tag{31}$$

The time derivative of the energy norm is found using a simple forward difference. Finally, the growth rate is the time rate of change of the energy norm, divided by the energy norm:

$$\sigma(t)=\frac{1}{K}\frac{dK}{dt} \tag{32}$$

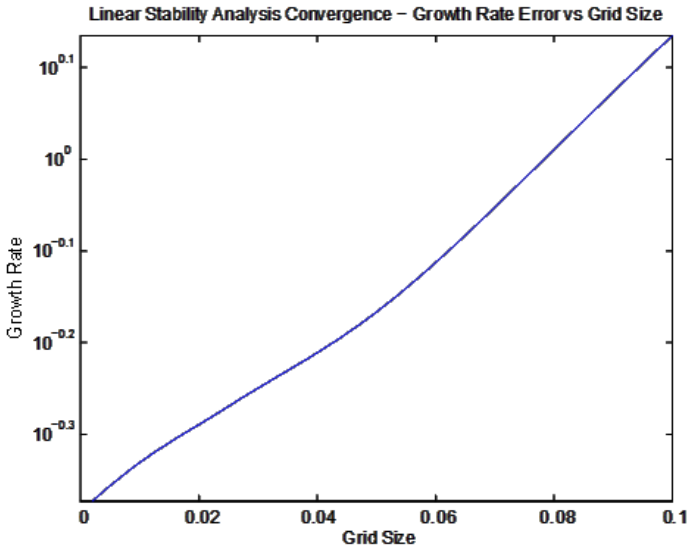

Figure 2: Convergence plot for error in growth rate with reducing mesh grid size

In order to ensure the solution is adequately resolved spatially, it is necessary to run the simulation for reducing grid sizes and check that the results tend towards a converged state. Figure 2 shows the convergence in relative error to growth rate with a reduction in mesh grid size. It is promising to see that the error does decrease asymptotically towards a true solution, noted by the linear curve on the semilogarithmic axes. Final runs are simulated with a mesh size of 1.0 millimeter as this provides a good accuracy to computational speed ratio. For a given Pe_T, R and λ the growth rates σ corresponding to a range of wave numbers m are simulated. The transient behavior of the growth rates is complex. The general trends observed are initially a sharp rise, followed by asymptotic decay. This behavior can be explained by noting that the base state velocity is not constant but decays as ~1/r as the front moves out radially. Thus the instability for each azimuthal mode decays with time after reaching a local maximum. Linear stability analysis predictions are only valid for short times, due to non-linear effects becoming more important as the perturbation grows at later times. Hence, the maximum growth rate during the time period for each wave number is recorded. Finally, maximum growth rate is plotted against wave number for three parameters: Péclet number Pe, log-mobility ratio R and thermal lag coefficient λ. For each case one parameter is varied, while keeping all others constant. This allows critical parameters to be determined.

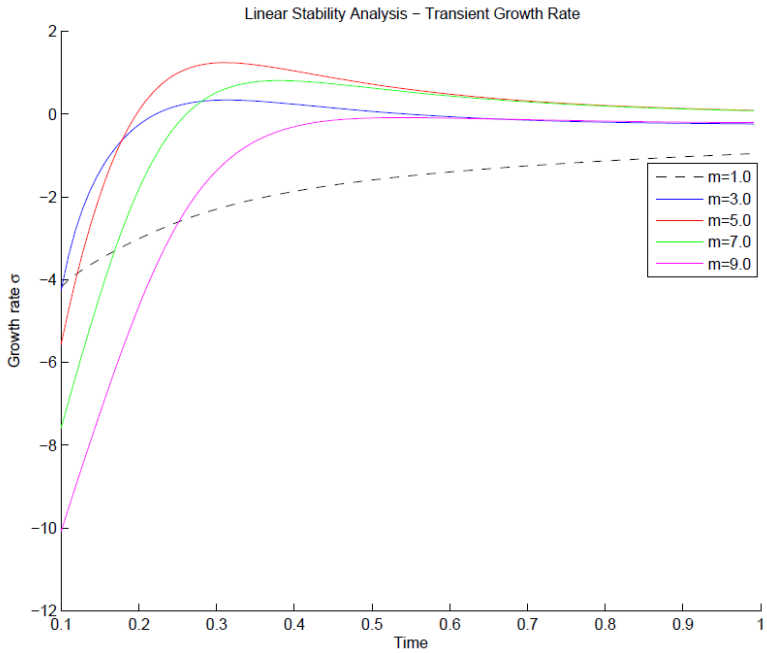

Figure 3: Transient curves for growth rates over a range of wave numbers (m). P eT = 100, R = 0.86, λ = 0.6

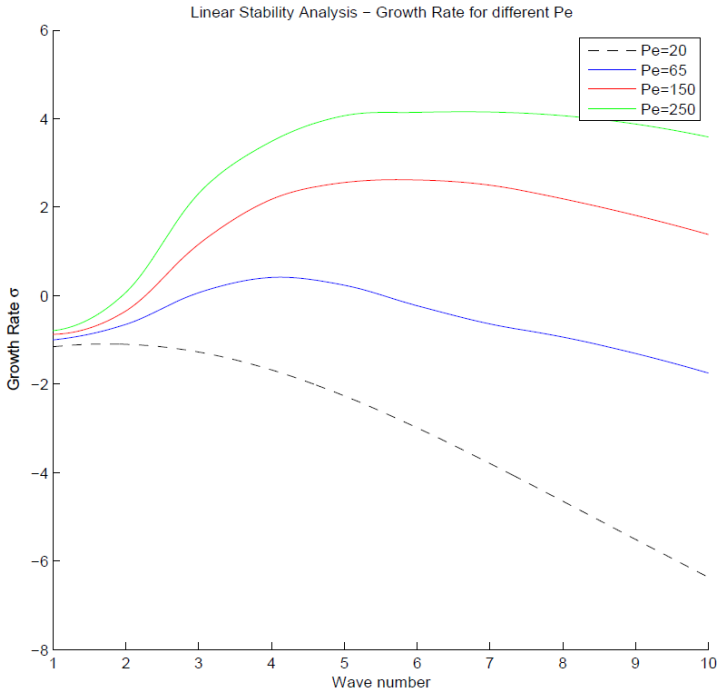

Figure 4: Maximum growth rates vs wave number for a range of Péclet numbers. R =0.86, λ = 0.6

Figure 4 shows the growth rates corresponding to a range of wave numbers for a selection of Péclet numbers. If the growth rates for all wave numbers are negative, then viscous fingering instability is not likely to occur, and the system is stable. This is the case for Péclet numbers less than approximately 60. Figure 4 shows for *Pe*= 20, all growth rates are negative. Above this critical Péclet number Pe_c, the growth rate is positive for some wave numbers, with a single most unstable wave number.

This is called the critical wave number mc, and it predicts which unstable mode will grow fastest, and thus dominate the viscous fingering displacement pattern. For *Pe*= 65, the critical wave number $m_c \approx 4$. Thus in one quadrant of the injection domain, we expect one large finger to form. For larger *Pe*, there is no distinct mc but rather a range of wavenumbers with similar growth rates. In this case we expect a range of fingering patterns to develop in the full numerical simulations, due to non-linear effects.

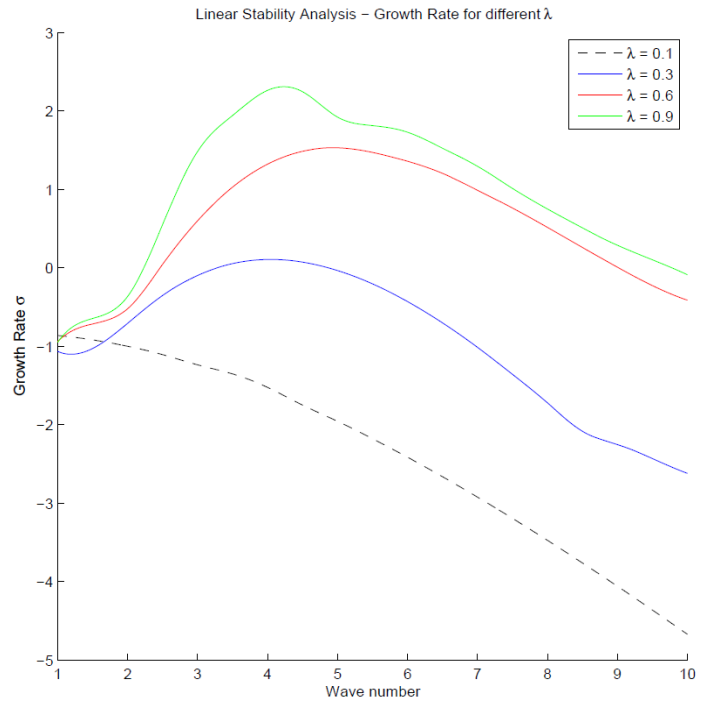

Figure 5: Maximum growth rates vs wave number for a range of thermal lag coefficients λ. (Pe_T = 100, R = 0.86)

The stabilising effect of the thermal lag coefficient λ is investigated. Figure 5 shows that for λ less than 0.3, the reinjection is stable. A low thermal lag coefficient corresponds with low porosity rock, as the volumetric heat capacity of water and rock are fixed for a homogeneous reservoir. An increase in λ tends to increase the instability. This follows logically. Advective processes

due to fluid flow are weaker in less porous rock compared with the diffusion of heat through the rock. These results also agree with the findings of Islam and Azaiez (2010a).

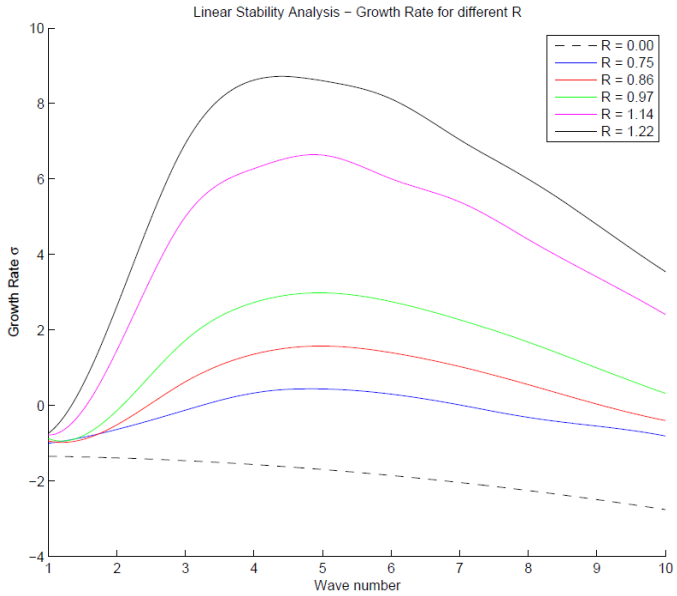

Figure 6: Maximum growth rates vs wave number for a range of log mobility ratios R ($Pe_T = 100$, $\lambda = 0.6$)

Finally, the effect of the log-mobility ratio is tested. The values for R correspond to various typical combinations of injection and native reservoir temperatures. For example, $R = 0.86$ corresponds to reinjection water with enthalpy 850 kJ/kg, temperature 200 ºC, and a reservoir temperature of 20 ºC. $R = 0$ describes two fluids with identical viscosity. Figure 6 shows that the system is stable for log-mobility ratios less than 0.75. Theory for the simple Hele-Shaw cell experiment predicts instability for any $R > 0$. However, in a geothermal reservoir there are more stabilising effects present to prevent instability for slightly adverse log-mobility ratios. Growth rates increase with larger log-mobility ratios.

3. NUMERICAL MODEL

3.1 Tough

The geothermal simulator TOUGH2.2 (Pruess et al., 1999) is used to perform numerical simulations in this project. The analysis is focussed on the flow of hot water injected from a single point source into a cold reservoir. TOUGH2.2 solves the mass and energy balance equations derived from the integral form of the conservation equations discussed in section 2. The spatial and temporal discretisation of these equations is an integral finite difference method (IDFM) (Pruess et al. 1999). The coupled non-linear equations are solved iteratively with the Newton-Raphson method. First order implicit time stepping ensures unconditional stability. The computational domain employed within TOUGH2.2 is a structured uniform Cartesian mesh. Gravity is not a variable of interest in this study, thus the domain is only one cell thick in the vertical direction. The resulting flow is essentially two-dimensional. The standard finite difference stencil used in TOUGH2.2 simulations is a five-point stencil. In this case, each block in the model is connected to four surrounding blocks in the vertical and horizontal directions. An improvement to this standard mesh is presented in Figure 7. Figure 7a shows the computational domain used in TOUGH2.2.

The numerical model is set-up to exploit symmetry in the radial configuration of the problem to improve computational efficiency. Thus one quarter of the circular domain is sufficient for simulations. Boundary conditions are prescribed implicitly in TOUGH2.2 as shown in Figure 7a. Top and right-hand boundaries are specified as no-flow boundaries. Left and bottom are open boundaries that allow fluid flow to penetrate by assigning very large volumes to these boundary blocks.

3.1.1 Geothermal Reservoir Parameters

Rock properties in well studied geothermal reservoirs are determined from field measurement data. The non-dimensional parameters identified in section 2 are used here to scale down our numerical solutions. A suitably fine grid is required to reduce numerical discretisation errors. It is preferable to work with non-dimensional variables during analysis. As rock and fluid properties are fixed, the parameter to be scaled to simulate various non-dimensional Péclet numbers will be the flow rate. Typical problem parameters and assumptions are given. Later it is useful to re-dimensionalise these non-dimensional numbers to determine the values of the parameters within in order to produce meaningful real-world results. Typical parameters are presented in Table 1 below.

Table 1: Typical geothermal reservoir parameters

Variable	Symbol	Equation	Value	SI Unit
Mass injection rate	$\dot{m}$		1.0×10^{-5}	$\mathrm{kg\,s^{-1}}$
Injection enthalpy	H		850	kJ kg-1
Injection temperature	T_1		200	°C
Injection viscosity	μ_1		1.364×10^{-4}	$\mathrm{kg\,m^{-1}\,s^{-1}}$
Depth of porous media	d		1.0×10^{-3}	m
Reservoir porosity	ϕ		0.3	[-]
Reservoir fluid temperature	T_∞		20	°C
Reservoir fluid viscosity	μ_∞		9.98×10^{-4}	$\mathrm{kg\,m^{-1}\,s^{-1}}$
Log mobility ratio	R	$\ln(\mu_\infty)/(\mu_1)$	0.86	[-]
Water density	ρ_w		1000	$\mathrm{kg\,m^{-3}}$
Rock density	ρ_w		2600	$\mathrm{kg\,m^{-3}}$
Volume injection rate	Q	$\dot{m}/\rho_w/d$	1.0×10^{-5}	$\mathrm{m^2\,s^{-1}}$
Specific heat of water	$C_{P,w}$		4184	$\mathrm{J\,kg^{-1}\,K^{-1}}$
Specific heat of rock	$C_{P,s}$		900	$\mathrm{J\,kg^{-1}\,K^{-1}}$
Thermal conductivity of water	k_w		0.58	$\mathrm{W\,m^{-1}\,K^{-1}}$
Thermal conductivity of rock	k_s		2.50	$\mathrm{W\,m^{-1}\,K^{-1}}$
Thermal diffusivity of water	$D_{T,w}$	$k_w/\rho_w C_{P,w}$	1.387×10^{-7}	$\mathrm{m^2\,s^{-1}}$
Thermal diffusivity of rock	$D_{T,s}$	$k_s/\rho_s C_{P,s}$	1.068×10^{-6}	$\mathrm{m^2\,s^{-1}}$
Average thermal diffusivity	D_T	$\phi D_{T,w} + (1-\phi) D_{T,s}$	7.895×10^{-7}	$\mathrm{m^2\,s^{-1}}$
Thermal Péclet number	Pe_T	Q/D_T	12.7	[-]

Flow rate: The rate at which fluid is injected into the reservoir from the bottom-left corner is the major advective force.

Unless otherwise stated, the log-mobility ratio tested in simulations is R= 0.86, for 850 kJ kg^{-1} injection enthalpy and 20 ºC reservoir temperature. There exists a critical Péclet number for the onset of fingering instability for each mobility ratio. These parameters will be investigated in this report with the use of numerical simulations.

3.2 Homogeneous Viscous Fingering

This section studies miscible displacements in homogeneous porous media. Rock properties of thermal conductivity, density, specific heat, and permeability are kept constant throughout the reservoir. Viscous fingering instability is governed by the Péclet Number, *Pe*, and the log mobility ratio, *R*. Numerical discretisation errors inherent in the TOUGH2.2 package restrict the observable conditions for viscous fingering in a homogeneous reservoir. Explanation is given as to the origins of this numerical phenomena and a method is presented to minimise its effect. Several methods to initiate fingering in a homogeneous reservoir are proposed. Linear stability analysis results are related to TOUGH2.2 simulation results.

3.2.1 Grid Orientation Effect

The numerical predictions are highly sensitive to the finite difference scheme employed, and can lead to the simulator converging towards different solutions (Fitzgerald and Shook 1994). Kozdon et al. (2009) has also investigated upwind transport schemes for simulating adverse mobility ratio displacements in porous media, and reports that the results are very sensitive to discretisation errors. This phenomenon is known as Grid Orientation Error (GOE). Both numerical and physical diffusive processes are present. Shubin and Bell (1984) report that most numerical techniques used to solve adverse mobility ratio displacement problems yield excessively smeared fronts, and a degree of spatial distortion. This has important implications for the application of TOUGH2.2 to solving reinjection problems where viscous fingering is expected. The numerical dispersion causes the flow to behave similar to one with a much lower Péclet number, due to extra diffusive processes competing with advective processes. The TOUGH2.2 solver takes 100% upstream weighting of flux terms at the front to avoid time-step limitations, and to achieve unconditional stability (Peaceman and Rachford, 1962). This results in an artificial dispersion term to the transported quantities in the form (Ewing 1983)

$$d = -\frac{\Delta x}{2}\frac{\partial^2 T}{\partial x^2} - \frac{\Delta y}{2}\frac{\partial^2 T}{\partial y^2} \tag{33}$$

where d is the numerical dispersion term, Δx and Δy computational mesh size.

This expression shows that there are different amounts of dispersion in the x and y directions, based on the discretisation scheme. Thus the artificial dispersion term d is directionally dependent, explaining the presence of GOE. It is useful to identify the source of the numerical error in order to isolate the physical instability within the simulations. We wish to allow the unstable characteristics of the geothermal system to trigger the instability, rather than the numerical errors in the simulation formulation. Kozdon et al. (2009) offers three avenues to reduce GOE:

1. Use a higher order scheme: Total Variation Diminishing (TVD) or Essentially Non- Oscillatory (ENO)

2. Use an adaptive scheme that predicts the preferred direction of transport

3. Extend the discretisation scheme from the standard five-point to a nine-point scheme (both first order)

(Chen et al. 1993b) reported that a nine-point finite difference scheme reduces GOE. The numerical dispersion tensor is rendered invariant to the orientation of the coordinate system using a nine-point stencil. Yanosik and McCracken (1979) described the development of a nine-point finite difference scheme for square grid networks used in reservoir simulators.

3.2.2 Thermal Shock

It is found that TOUGH2 simulator cannot solve for high enthalpy rates. This is due to the large temperature jump induced across the thermal front. The solver algorithm reduces to vanishingly small time-steps attempting to resolve the large gradients across the 'shock' type thermal jump. Thus, there is an upper limit for the injection enthalpy rate that can be simulated. This upper limit is estimated to be an enthalpy of 850 kJ kg^{-1} for water at 200 °C. In order to force higher mobility ratios, the temperature of the reservoir must be reduced.

3.2.3 Nine Point Finite Difference Grid

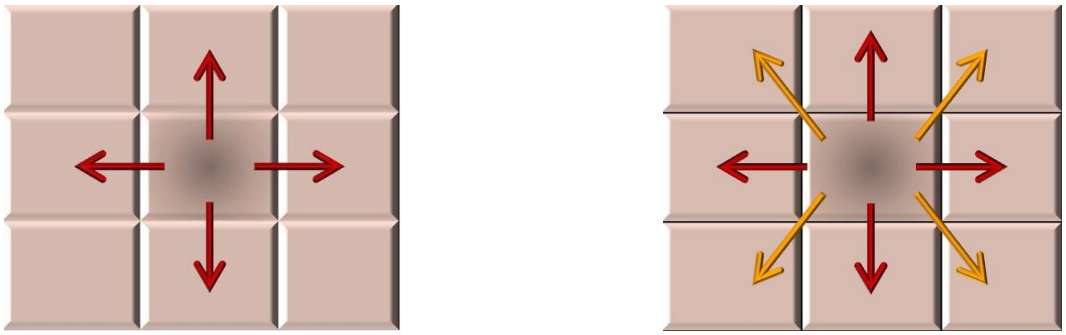

(a) Five point scheme (b) Nine point scheme

Figure 7: Integrated finite difference schemes calculate flows from connected adjacent blocks. The new nine point scheme allows for flow connections between diagonally adjacent blocks.

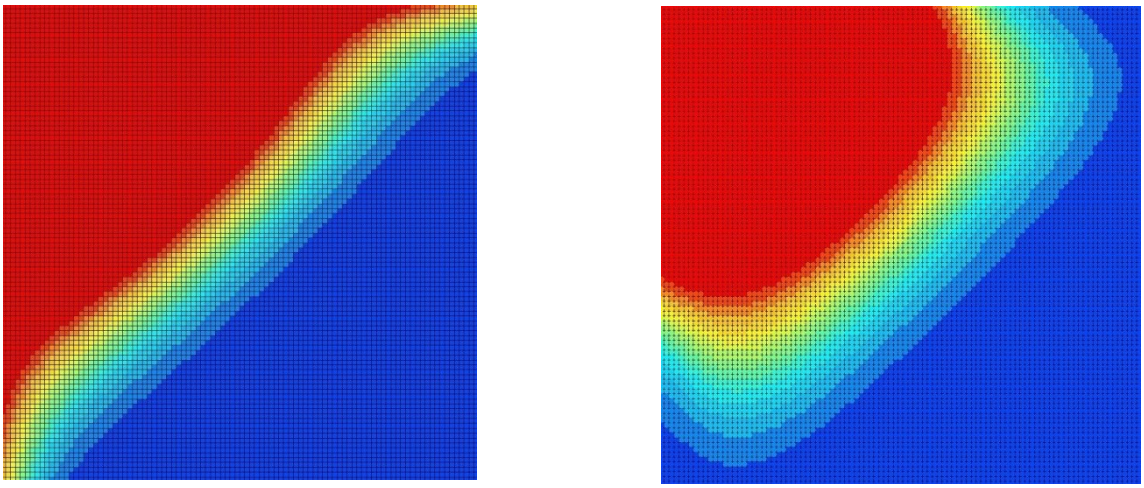

(a) 5-point stencil. (b) 9-point stencil.

Figure 8: TOUGH2.2 modeling results showing: Temperature profile of a quarter-section of the reservoir for two finite difference stencils.

The first approach to isolate the physical instability from undesirable numerical instability is to improve the finite difference grid upon which TOUGH2.2 is based. The four diagonally adjacent blocks to each control volume are assigned as additional connections in the TOUGH2.2 input data file. The nine-point finite difference stencil was developed using Excel VBA, for ease of reproducing different mesh sizes. A letter grid is generated from a numeric matrix using a recursive algorithm. Each block is assigned connections to all eight surrounding blocks by including the additional four diagonal directions. Total surface area contact between adjacent blocks is conserved for five and nine point schemes. Two simulations were run with parameters stated in Table 1. Figure 8a uses a five-point stencil; Figure 8b uses a nine-point stencil. The two models are allowed equal amount of time to evolve. Our results for homogeneous fingering shown in Figure 8b agree very closely with those reported by Yanosik and McCracken (1979). This verifies that our nine-point scheme is working correctly. However, despite the reduction in GOE, nine-point schemes are still only accurate to first order, and still require a fine mesh for adequate resolution and convergence. Initial observations find that a notable thermal boundary layer forms between the fluid front and the far-field reservoir domain. The width of the thermal

boundary layer is dependent on the thermal conductivity and specific heat of the rock. However, at a lower flow rate and conductivity (maintaining same overall *Péclet* number), the fingering pattern is identical, but with a more narrow thermal boundary layer. A lower flow rate implies more time is taken for the finger to reach the same extent. If significant numerical dispersion were to occur, a simulation with more time steps would be expected to exhibit more pronounced smearing of the thermal front due to numerical dispersion. As this is not the case, it is assumed that the width of the thermal layer is solely dependent on the thermal properties of the rock and fluid, rather than the numerical method, in this case.

Figure 8a shows fingers forming in the *x* and *y* directions. In contrast, Figure 8b displays a large finger aligned with the diagonal flow direction. Similar viscous fingering displacements results occur in super critical conditions, and display the same grid orientation dependence Fitzgerald and Shook (1994). The evolution of the interface is therefore heavily dependent on the finite difference stencil used.

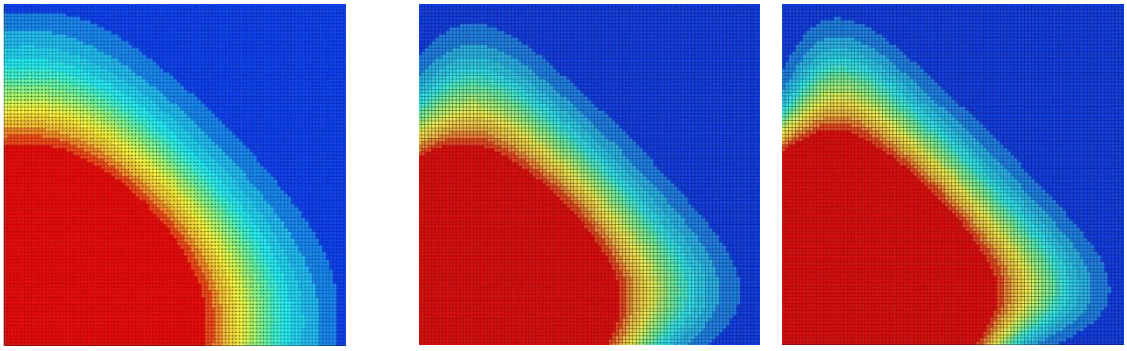

(a) Pe = 125 (b) Pe = 300 (c) Pe = 650

Figure 9: TOUGH2.2 modeling results showing: Temperature profiles at various Péclet numbers. Notice the transition from an azimuthally-symmetric front (left) to viscous fingering (right). (a) Shows marginal stability (Q=1.0 × 10^{-4} m^2 s^{-1}), (b) Transition (Q=2.4 × 10^{-4} m^2 s^{-1}), (c) Fully developed (Q=5.1 × 10^{-4} m^2 s^{-1}).

As identified in section 2, a critical *Péclet* number exists for the onset of fingering. Figure 9 shows the form of this finger over a range of *Péclet* numbers. For this reservoir, the thermal diffusion coefficient D_T = 7.9 × 10^{-7} m^2 s^{-1}, and flow rates range between Q = 1.0 × 10^{-4} m^2 s^{-1} and Q = 1.0 × 10^{-3} m^2 s^{-1}.The critical *Péclet* number estimated in linear stability analysis was *Pe*=65 for *R* = 0.86. The critical flow rate measured here is Q = 2.0 × 10^{-4}, with *R* = 0.86. Thus the critical *Péclet* number is Pe_c=125. Thus the Pe_c predicted by TOUGH2.2 is approximately twice the Pe_c predicted by linear stability analysis. It should be noted that Pe_c cannot be determined exactly due to the artificial numerical dispersion and parallax error viewing results at different times. Thus there remains a level of uncertainty around the precise critical values. However, this result aligns with our predictions that the extra numerical diffusion will stabilise fingering for higher *Péclet* numbers that would be unstable otherwise.

3.2.4 Perturbation Forcing

The second technique proposed to initiate fingering is to carry out a perturbation analysis using TOUGH2.2. The temperature profile for a stable simulation run is perturbed by a small amplitude sinuisoid locally about the front. It is used to analyze whether the forced perturbation grows or decays with time.

$$T_b(\xi(r,t)) = \frac{\int_0^{\xi} s^{Pe_T\lambda-1} e^{-\frac{s^2}{2}} ds}{\int_0^{\infty} s^{Pe_T\lambda-1} e^{-\frac{s^2}{2}} ds} \qquad \xi = r\frac{Pe}{2t} \tag{34}$$

Equation 34 is the axisymmetric temperature state that was derived in section 2.2.3. The instability is localised about the thermal front interface, thus the perturbation to the basic state, $T = T_B + \exp im\theta\, T'$ must be applied only about the radius of the interface as it has developed after a small time of injection. The thermal front position is about $\xi = \sqrt{Pe}$ thus the radius is $r_T(t) = \sqrt{2t}$ (Tan and Homsy 1987). A perturbation in the form of an arbitrary Gaussian pulse of amplitude A, wave number m, standard deviation (width) c is applied to the basic temperature state about the thermal front position r_T after a small time. Several wave numbers are tested to determine which is most unstable.

$$T(t,r,\theta) = T_b + Ae^{im\theta} e - \frac{(r - r_T(t))^2}{2c^2} \tag{35}$$

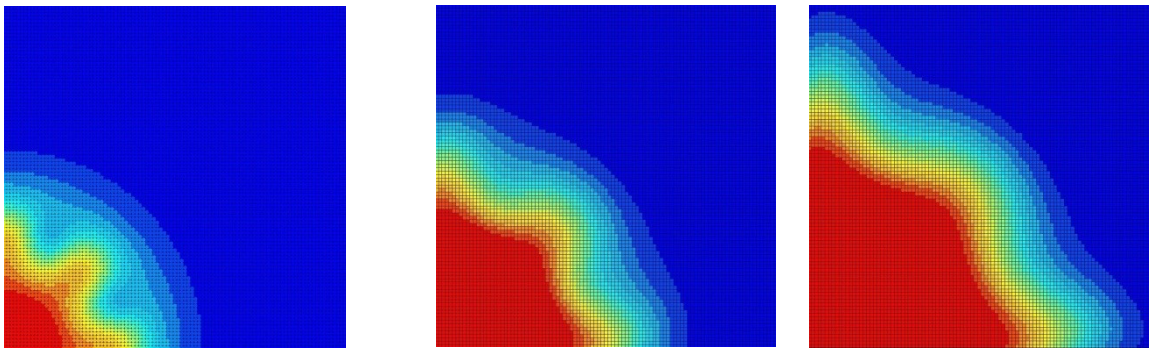

(a) 0 seconds (b) 1 seconds (c) 2 seconds

Figure 10: TOUGH2.2 modeling results showing: Development of temperature profile at various times with artificial perturbations

The temperature distribution is generated in *MATLAB*, and written to an initial conditions file for simulation in *TOUGH*2.2. Figure 10 shows that with time the initially perturbed temperature profile tends towards the same wavelength of the unperturbed finger. The amplitude of the fingers decays over time as the moving front spreads. Thus TOUGH2.2 is insensitive to initial conditions. Flow and fingering displacement patterns are dominated by input parameters defining *Péclet* number and log-mobility ratio.

3.3 Heterogeneous Fingering

In a real geothermal reservoir, heterogeneities in the porous rock matrix are common. Variations in field permeability cause new fluid flow phenomena that are not observed in a homogenous reservoir model. Several authors (Sajjadi and Azaiez 2012; De Wit and Homsy 1997; Riaz and Meiburg 2004) have investigated the effects of heterogeneity on thermo-viscous fingering and propose several models for possible permeability distributions. Sajjadi and Azaiez (2012) identified two specific mechanisms that cause viscous fingering in heterogeneous porous media: an adverse log-mobility ratio, and channeling. These mechanisms have different levels of influence depending on the variance and correlation length scales of heterogeneity perturbations.

3.3.2 Randomly Distributed Permeability

The second model assumes a randomly perturbed permeability field. k_x and k_y for each block belong to a log-normal distribution. The log-normal distribution $k_{x,y} \sim \ln(\tau, \sigma^2)$ takes the mean permeability k_0 and variance v of the permeability to calculate the distribution mean τ and standard deviation σ (Forbes et al. 2011).

$$\tau = \log(k_0^2 / \sqrt{v + k_0^2}) \qquad \sigma = \sqrt{\log(v / k_0^2 + 1)} \tag{36}$$

The results for this field show a chaotic fingering displacement pattern as expected:

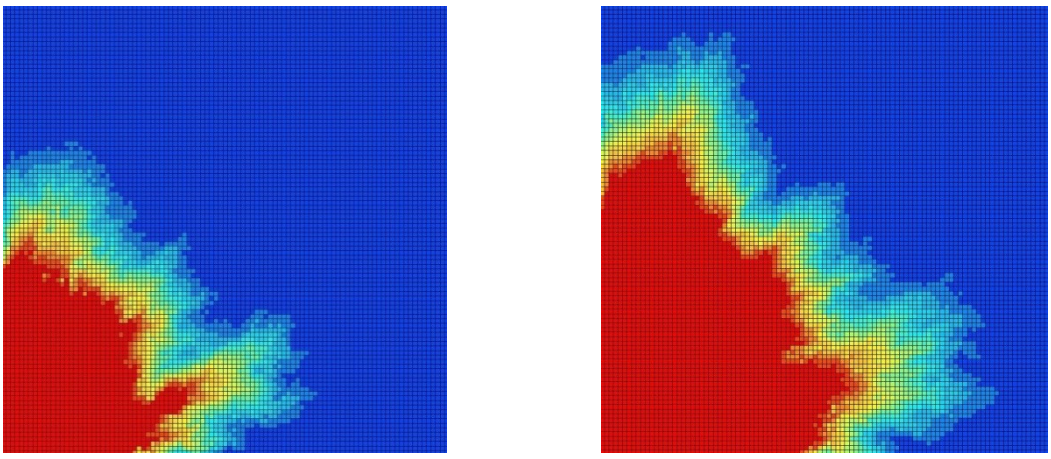

(a) (b)

Figure 11: TOUGH2.2 modeling results showing: Temperature profiles for injection displacements in a log-normally distributed permeability field, $k_0 = 0.1$, $v = 0.3$. (a) t=13 sec (b) t=23 sec

Next, two random permeability distributions are compared. A simple uniformly distributed pseudo-random permeability field generated with MATLAB's *rand* function models the case of small perturbations about the mean permeability. The variance of perturbations is equal for both log-normal and pseudo-random fields. Despite different seedings to these distributions, similar finger formations are produced. These are compared to the homogeneous case for reference in Figure 12a.

Studying the temperature profiles in Figure 12 closely, three fingers form in each plot. For the homogenous case, the finger on the diagonal is very subtle and does not grow as fast as fingers in the *x* and *y* directions. Given a perturbed permeability distribution,

these three fingers grow at similar rates. The log normal distribution produces a far more chaotic thermal front when compared with the uniform random distribution of permeability. The pseudo-random distribution appears to trigger a larger dominant wavenumber of perturbation growth than the homogeneous case. Figure 12a shows a very small disturbance growing along the diagonal. With the pseudo-random distribution, this disturbance is a fully grown finger.

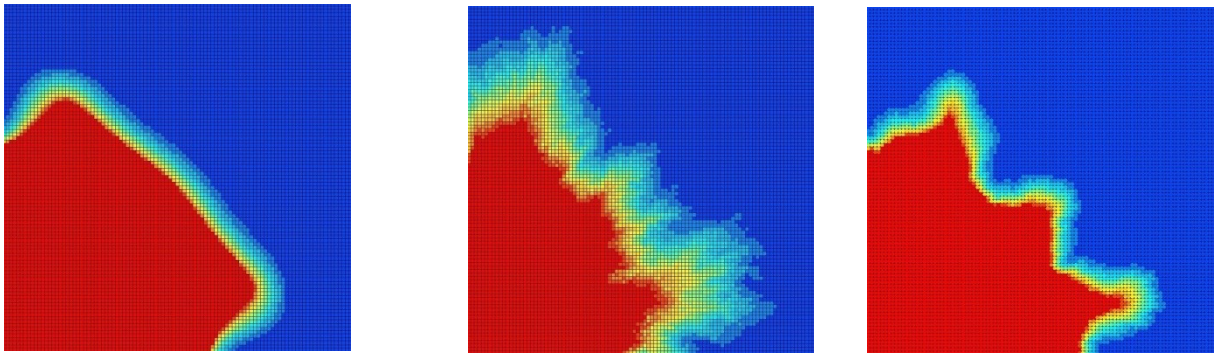

(a) Homogeneous (b) Log-normal (c) Uniform pseudorandom

Figure 12: TOUGH2.2 modeling results showing: Temperature profiles for injection displacements in various distributed permeability structures. The mean permeability for all three cases is $k_x = k_y = 100mD$.

3.3.3 Periodic Permeability

The third heterogeneity model is a periodic permeability field. A model used by (Riaz and Meiburg 2004; De Wit and Homsy 1997):

$$k(x,y) = k_0 \exp\{\gamma \cos(2\pi nx)\cos(2\pi qy)\} \tag{37}$$

where k_0 is the mean permeability as in equation 36, γ is the amplitude or variance of the heterogeneity, n and q are the wave numbers of the periodicity, taken here as equal. In order to implement this periodic plane in TOUGH2.2, permeabilities must be systematically applied to each grid block in the finite volume grid. One 2D period of the periodic pattern is discretised into a 5-by-5 mesh. Permeability at each node in this grid is stored in a separate rock type. Each grid block in the TOUGH2.2 data file is assigned the correct rock type to produce the overall periodic permeability field.

Results from TOUGH2.2 do indeed show heterogeneous fingering displacement patterns occurring. Figure 14 demonstrates the transient nature of finger formation. Initially three fingers form; soon after the outer fingers undergo tip splitting. Lajeunesse and Couder (2000) finds that for viscous fingers governed by the Saffman-Taylor instability, local destabilisation of the front occurs, resulting in splitting of the tip, and two new branches spread separated by a channel. Analogously, this process also occurs in the case of heterogeneous fingering whereby fingers routinely split and branch off, destabilised by the permeability perturbations. These results are validated against extensive work of Riaz and Meiburg (2004). Results for similar correlation scale and variance of the periodic permeability field show very similar displacement patterns.

Relating back to earlier discoveries between five and nine point finite difference grid in Figure 7, the two schemes are compared for the case of a periodic permeability field. Before differencing schemes are compared, it is worth noting that the nature of the periodic permeability field facilitates diagonal flow more than flow in x and y directions due to alignment of high permeability centres. This alignment is only a grid orientation effect, thus the performance of the two finite difference stencils in reducing GOE will be put to the test.

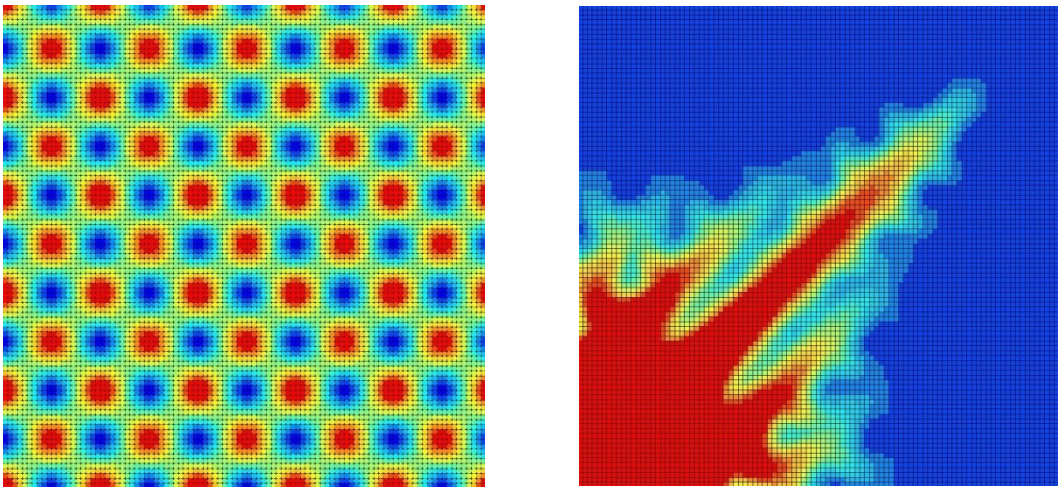

(a) (b)

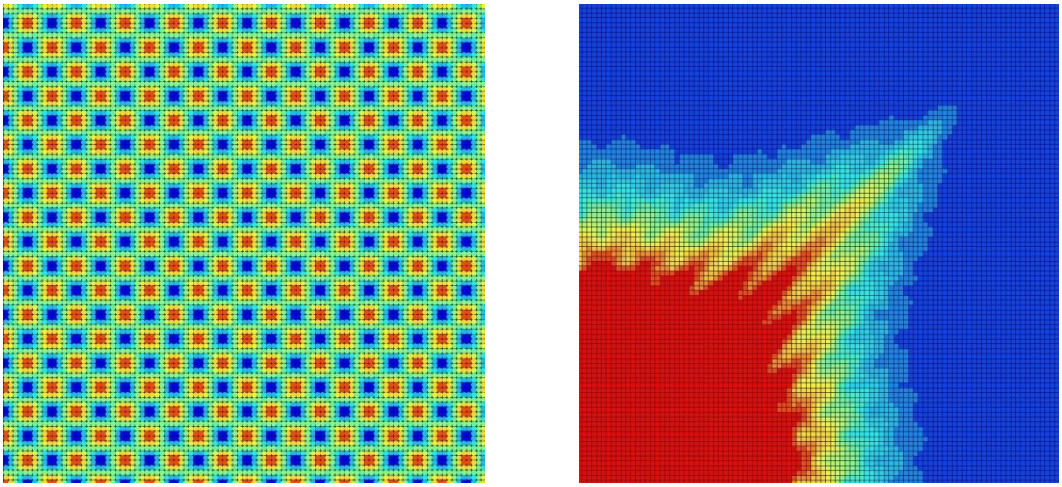

(c) (d)

Figure 13: Periodic permeability fields as per equation 38 as implemented in TOUGH2.2. Isotropic permeability magnitudes range from 300mD (red) to 30mD (blue) for (a) λD= 5, σln(κ) = 1.0 (b) (a) λD = 10, σln(κ) = 1.0. Associated temperature profiles showing fingering displacement patterns in (c) *HI*=5 (d) *HI*=10

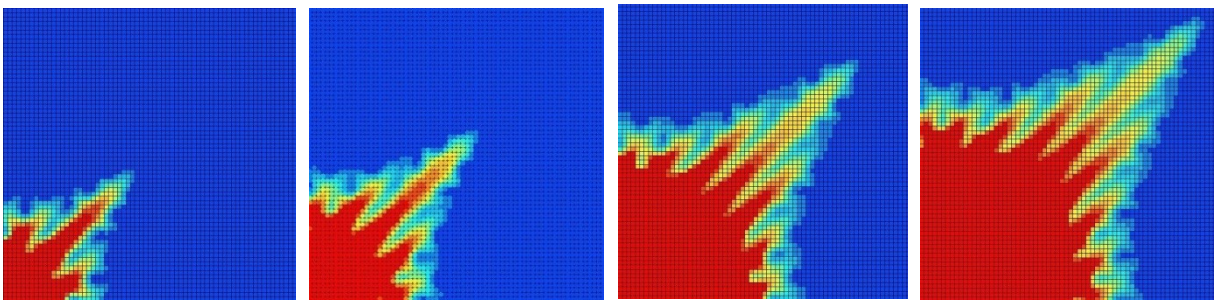

(a) 1 second (b) 5 seconds (c) 20 seconds (d) 54 seconds

Figure 14: TOUGH2.2 modeling results showing: Temperature profiles for injection displacements in a spatially periodic permeability field, shown at different times in development.

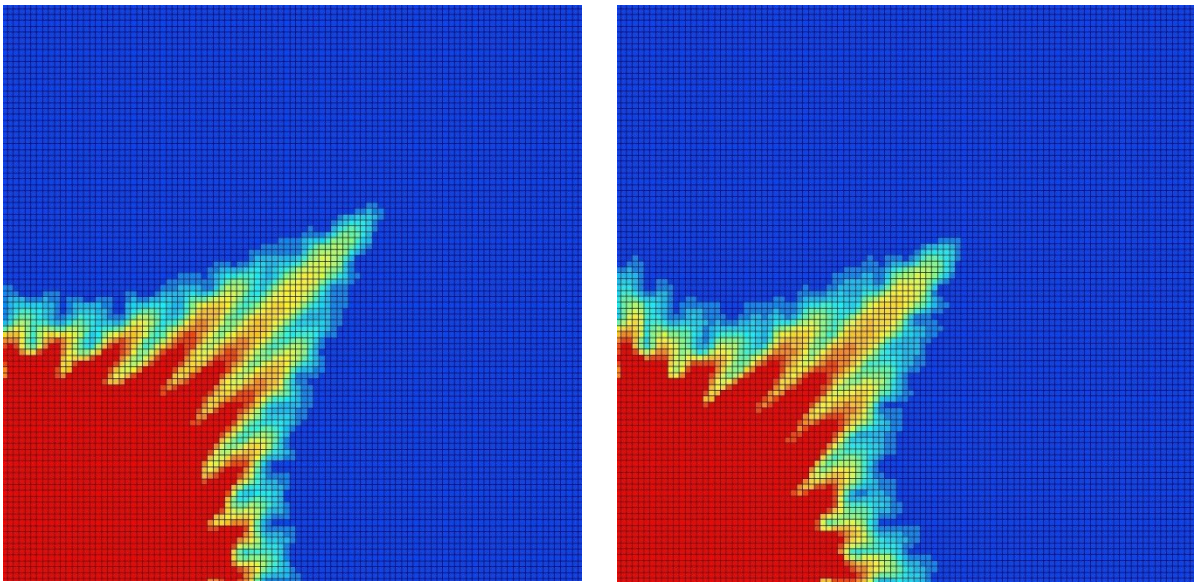

(a) (b)

Figure 15: TOUGH2.2 modeling results showing: Temperature profiles for injection displacements in a spatially periodic permeability field. (a) Five point differencing grid (b) Nine point differencing grid

At equal times after the start of injection, the displacement pattern is slightly different. The nine-point grid, aiming to reduce grid-orientation-effect (GOE), allows more flow in the diagonal direction. The five-point grid allows more flow in the vertical and horizontal grid directions. However, the difference between these profiles is much less pronounced than in Figure 8. Araktingi and Orr Jr (1993) introduced the heterogeneity index to help distinguish between viscous fingering driven by adverse mobility ratios, and heterogeneous fingering dominated by the structure of the permeability field. The heterogeneity index (HI) is defined as:

$$HI = \sigma^2_{\ln(k)} \lambda_D \tag{38}$$

where σln(k) is the standard deviation of log permeability, thus $\sigma^2_{\ln(k)}$ is the variance of log permeability, λ_D is the correlation length scale nondimensionalised by flow length. According to Araktingi and Orr Jr (1993), if the heterogeneity index is sufficiently large, then the permeability distribution dominates, and finger formation is the same regardless of the viscosity contrast.

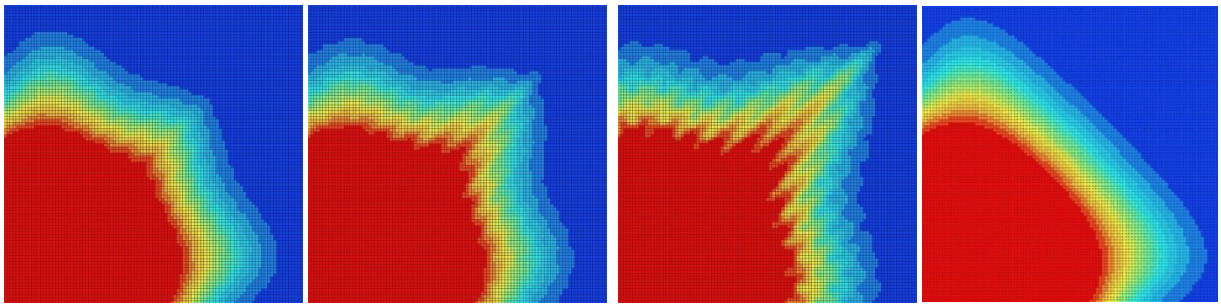

(a) Homogeneous (b) *HI*=0.2 (c) *HI*=2.0 (d) *HI*=5.0

Figure 16: TOUGH2.2 modeling results showing: Temperature profiles for injection displacements in a spatially periodic permeability field with a range of heterogenity indices (*HI*)

To illustrate this, a periodic permeability field with various heterogeneity indices is investigated. The results appear in Figure 16, compared with the homogeneous case (Fig 16a) for reference. As *HI* tends to zero, the heterogeneous fingering displacement patterns tend towards the fingering patterns observed with homogeneous reservoir properties. This experiment shows that heterogeneities in the porous media are dominated by the adverse mobility ratio for $HI < 0.2$, there is a transition region for $0.2 < HI < 2.0$, and heterogeneities dominate the displacement pattern for $HI > 2.0$.

4. CONCLUSIONS

Hydrodynamic instability analysis and geothermal reservoir simulation have shown that viscous fingering can occur in geothermal reservoirs during reinjection. Extensive work has shown the presence of viscous fingering in Hele-Shaw cells, petroleum reservoirs and other environmental flows. However, until now it has not been clear whether viscous fingering can occurs in hot water (liquid dominated) geothermal reservoirs.

Use of hydrodynamic instability theory helped us to gain qualitative insights into the parameters which affect the onset of viscous fingering in homogeneous porous media. The stability criterion for the simplest case of Saffman-Taylor instability determined that miscible displacements are unstable for any mobility ratio greater than unity, such that the injected fluid is less viscous than the native fluid. A linear stability analysis has been performed for a radial source flow in porous media producing a single thermal front. The governing equations of continuity and advection- diffusion, combined with Darcy's Law define the system. Stable base state solutions for temperature and velocity are perturbed, and we analysed whether these perturbations grow or decay, thus determining the stability of the system. The Method of Lines is used to time-step the perturbations and calculate growth rates from an energy norm, as it is proven that the QSSA does not apply for a spatially varying base solution. Linear stability analysis results provide two useful pieces of information. Firstly, whether any given parameters are likely to lead to instability. A wide selection of parameters may be varied, while keeping all others constant. The most important parameter that affects the onset of viscous fingering is the Péclet number. An increase in the Péclet number almost always acts to increase the instability. An increase in the thermal lag coefficient, that is the ratio of volumetric heat capacity of fluid to both fluid and rock, also tends to increase the instability. An increase in the mobility ratio always increases the growth rate of perturbations. The most unstable wave number increases with an increase in Péclet number. Thus for lower Péclet numbers, fewer large fingers will form, whereas for larger Péclet numbers many fingers in the spectrum may grow. Secondly, results show which wave numbers will dominate. The wave number corresponding to the maximum growth rate predicts the shape of the fingering displacements. For moderate Péclet numbers, this most unstable wave number is $m \approx 4$. This prediction is easily validated by numerical simulations, and is shown to be accurate by the formation of one larger finger in the quarter domain. At larger Péclet numbers, there is a band of dominant wave numbers which compete, and appear as a superposition of modes in the TOUGH2.2 simulations.

Numerical simulations using TOUGH2.2 allowed for the full complexity of a geothermal reservoir to be modelled and provide an avenue for testing analytical stability criteria. Homogeneous reservoir simulations show the existence of large fingers forming for $Pe > Pe_c$. For $R = 0.86$, the critical Péclet number Pe_c=125. This equates to a critical mass flow rate of 2.0×10^{-4} kg/s for the given reservoir. This flow rate is for a very small scale reservoir, 10 cm×10 cm. This value can be scaled up for a full scale reservoir. The discrepancy between the numerical and analytical estimates for the critical Péclet number can be explained by the inherent numerical dispersion in approximating large derivatives at the thermal 'shock' front. Overall, they are shown to provide reasonably cohesive results. The rotationally variant numerical dispersion tensor causes large differences in displacement patterns for different finite difference stencils. Varying thermal properties of rock with fixed Péclet number does not alter fingering pattern, but affects width of the thermal boundary layer. Small perturbations to the permeability are sufficient to initiate fingering in TOUGH2.2. Growth in the amplitude of fingering perturbations is strongest initially. At longer times, these formations spread throughout the reservoir without becoming more unstable. This qualitative behaviour is parallel to that observed in the linear stability results for homogeneous instability.

Various permeability distributions are also investigated. Pseudo-random permeability accelerates the growth of modes that are only slightly unstable in the homogeneous case. Log-normally distributed permeability leads to chaotic fingering patterns, but the underlying structure still exhibits several most unstable modes. Periodic permeability can dominate mobility-driven fingering, and cause heterogeneous effects such as channeling and finger resonance. The heterogeneity index (*HI*) is shown to be a good measure for where heterogeneous fingering begins to dominate over mobility driven flow. When the product of permeability variance and correlation length scale exceeds 2.0, heterogeneous fingering is likely to occur regardless of the mobility ratio.

The nine point differencing scheme should be considered when setting the TOUGH2.2 grid in the target formations when modeling reinjection in geothermal reservoirs. However, such template can be dispersive due to transport along the diagonal grid connections. Given that fingering is controlled by Péclet numbers, log mobility ratio and the heterogeneity index (*HI*), which are difficult to quantify prior to starting the calibrating of a new model/field. It is recommended that both differencing schemes should be investigated as part of the mesh/grid independence study.

NOMENCLATURE

A	Viscosity contrast
C_p	Specific heat capacity
c	Standard deviation
ϵ	Small parameter used in asymptotic expansions
γ	Square root of variance
H	Enthalpy
HI	Heterogeneity index
L	Length
l	Longitudinal wave number
λ	Thermal lag coefficient, correlation length scale
K	Thermal Conductivity
k	Permeability
m	Wave number
M	Mobility ratio
n	Wave numbers of the periodicity in the x direction
μ	Viscosity (dynamic)
P	Reservoir pressure
p	Injected fluid pressure
q	Wave numbers of the periodicity in the y direction
Pe	Péclet number
ϕ	Porosity
Q	Volume flux rate
r	Radius measured away from well injection point
R	Log-mobility ratio
ρ	Density
σ	Standard deviation, growth rate
t	Time
T	Temperature
τ	Distribution mean
θ	Angle measured about central well injection point
U	Constant flow velocity
u	Fluid velocity
v	Variance
x, y	Spatial coordinates
ξ	Similarity coordinate
ζ	Perturbation amplitude

Subscripts

0	Initial, mean state
1	Injected fluid
∞	Native reservoir fluid
B	Basic state
c	Critical
D	Dimensional
r	Radial
T	Thermal
θ	Azimuthal

ACKNOWLEDGEMENTS

The authors would like to thank Mr. Yasir Al-Hilali for his help in formatting the manuscript.

REFERENCES

Araktingi, U. and Orr Jr, F. (1993), Viscous fingering in heterogeneous porous media, SPE Advanced Technology Series 1 (1), 71.

Cengel, Y. A., Turner, R. H. and Cimbala, J. M. (2012), Fundamentals of Thermal-Fluid Sciences, McGraw-Hill.

Chen, W., Durlofsky, L., Engquist, B. and Osher, S. (1993a), Minimization of grid orientation effects through use of higher order finite difference methods, SPE Advanced Technology Series 1(2), 43-52.

Chen, W., Durlofsky, L., Engquist, B. & Osher, S. (1993b), `Minimization of grid orientation effects through use of higher order _nite di_erence methods, SPE Advanced Technology Series 1(2), 43-52.

De Wit, A. & Homsy, G. (1997), Viscous fingering in periodically heterogeneous porous media. In formulation and linear instability, The Journal of chemical physics 107, 9609.

D.E.S. (2013), Geothermal, reservoir engineering and environmental stuids. URL: http://www.des.auckland.ac.nz/uoa/geothermal energy-research

Dias, E. O. & Miranda, J. A. (2011), Influence of inertia on viscous fingering patterns: Rectangular and radial flows, Physical Review E 83(6), 066312.

Ewing, R. E. (1983), The mathematics of reservoir simulation, Siam, Philadelphia.

Fitzgerald, SD, W. A. and Shook, M. (1994), `Viscous fingers in superheated. geothermal systems.

Forbes, C., Evans, M., Hastings, N. and Peacock, B. (2011), Statistical distributions, Wiley.com.

Homsy, G. (1987), `Viscous _ngering in porous media', Annual Review of Fluid Mechanics 19(1), 271-311.

Islam, M. & Azaiez, J. (2010a), Miscible thermo-viscous fingering instability in porous media. part 1: Linear stability analysis, Transport in porous media 84(3), 821-844.

Islam, M. and Azaiez, J. (2010b), Miscible thermo-viscous fingering instability in porous media. part 2: Numerical simulations, Transport in porous media 84(3), 845-861.

Jupp, T. & Woods, A. (2003), Thermally driven reaction fronts in porous media', Journal of Fluid Mechanics 484, 329-346.

Kaya, E., Zarrouk, S. J. & O'Sullivan, M. J. (2011), Reinjection in geothermal fields: Areview of worldwide experience, Renewable and Sustainable Energy Reviews 15(1), 47-68.35

Kim, M. C. (2012), Linear stability analysis on the onset of the viscous fingering of a miscible slice in a porous medium, Advances in Water Resources 35, 19.

Kozdon, J., Mallison, B. and Gerritsen, M. (2009), Robust multi-d transport schemes with reduced grid orientation effects, Transport in porous media 78(1), 47-75.

Lajeunesse, E. & Couder, Y. (2000), On the tip-splitting instability of viscous fingers, Journal of fluid mechanics 419, 125-149.

Lenormand, R., Touboul, E. & Zarcone, C. (1988), Numerical models and experiments on immiscible displacements in porous media. Journal of Fluid Mechanics 189(1), pp.165-187.

Nervous System (2011), Hele-shaw cell experiments. URL: http://vimeo.com/22212386

O'Sullivan, M. & Pruess, K. (1980), Analysis of injection testing of geothermal reservoirs, Technical report, California Univ., Berkeley (USA). Lawrence Berkeley Lab.

Peaceman, D. & Rachford, H. (1962), Numerical calculation of multidimensional miscible displacement, Old SPE Journal 2(4), 327-339.

Pritchard, D. (2004), The instability of thermal and fluid fronts during radial injection in a porous medium', Journal of Fluid Mechanics 508, 133-163.

Pruess, K., Oldenburg, C., and Moridis, G.: TOUGH2 User's Guide, Version 2.0. Report–43134, Lawrence Berkeley National Laboratory, Berkeley, CA (1999).

Riaz, A. and Meiburg, E. (2003), Radial source flows in porous media: Linear stability analysis of axial and helical perturbations in miscible displacements, Physics of Fluids 15, 938.

Riaz, A. & Meiburg, E. (2004), Vorticity interaction mechanisms in variable-viscosity heterogeneous miscible displacements with and without density contrast, Journal of Fluid Mechanics 517, 1-25.

Sa_man, P. & Taylor, G. (1958), The penetration of a fluid into a porous medium or Hele-shaw cell containing a more viscous liquid', Proc. R. Soc. Lond. A 245, 312-329.

Sajjadi, M. & Azaiez, J. (2012), Thermo-viscous fingering in heterogeneous media, in SPE Heavy Oil Conference Canada.

Scovazzi, G., Huang, H., Collis, S. & Yin, J. (2013), A fully-coupled upwind discontinuous galerkin method for incompressible porous media flows: High-order computations of viscous fingering instabilities in complex geometry, Journal of Computational Physics.

Shubin, G. & Bell, J. (1984), An analysis of the grid orientation effect in numerical simulation of miscible displacement, Computer methods in applied mechanics and engineering 47(1), 47-71.

Tan, C. & Homsy, G. (1987), Stability of miscible displacements in porous media: Radial source flow, Physics of Fluids 30, 1239.

Tan, C. & Homsy, G. (1988), Simulation of nonlinear viscous fingering in miscible displacement, Physics of Fluids 31, 1330.

Tan, C. & Homsy, G. (1992), Viscous fingering with permeability heterogeneity, Physics of Fluids A Fluid Dynamics 4(6), 1099.

Yanosik, J. & McCracken, T. (1979), A nine-point finite-difference reservoir simulator for realistic prediction of adverse mobility ratio displacements, Old SPE Journal 19(4), 253-262.